Received: 6 December 2021 | Revised: 9 February 2022 | Accepted: 9 February 2022

DOI: 10.1002/er.7770

RESEARCH ARTICLE

INTERNATIONAL JOURNAL OF ENERGY RESEARCH WILEY

Porous nanofibers comprising hollow Co_3O_4/Fe_3O_4 nanospheres and nitrogen-doped carbon derived by Fe@ZIF-67 as anode materials for lithium-ion batteries

Ki Cheon Nam[1] | Young Hoe Seon[2] | Parthasarathi Bandyopadhyay[1] | Jung Sang Cho[2] | Sang Mun Jeong[1]

[1]Department of Chemical Engineering, Chungbuk National University, Cheongju, Republic of Korea

[2]Department of Engineering Chemistry, Chungbuk National University, Cheongju, Republic of Korea

Correspondence
Jung Sang Cho, Department of Engineering Chemistry, Chungbuk National University, 1, Chungdae-Ro, Seowon-Gu, Cheongju-Si, Chungbuk 361-763, Republic of Korea.
Email: jscho@cbnu.ac.kr

Sang Mun Jeong, Department of Chemical Engineering, Chungbuk National University, 1, Chungdae-Ro, Seowon-Gu, Cheongju-Si, Chungbuk 361-763, Republic of Korea.
Email: smjeong@chungbuk.ac.kr

Funding information
Chungbuk National University Korea National University Development Project (2021)

Summary

Porous nanofibers comprising of Fe@ZIF-67-derived dual-phase Co_3O_4/Fe_3O_4 hollow nanospheres and N-doped graphitic C (N-GC) are prepared for high-performance lithium-ion battery anodes. Optimized ZIFs containing both Co and Fe ion nodes (Fe@ZIF-67) are prepared by the supplementation of additional Fe salt in the precursor solution of ZIF-67. The size of Fe@ZIF-67 is controlled by adjusting the pH value. Further, hollow-structured dual-phase Co_3O_4/Fe_3O_4 nanospheres in the structure are obtained through the mechanism involving Kirkendall diffusion nanoscale regime to as-spun fibers by performing simple heat treatments. The obtained unique nanostructure shows a high discharge capacity of 937 mA h g^{-1} after the 150th cycle at 0.1 A g^{-1} current density. Final discharge capacities of A300NF at different current densities of 0.1, 0.5, 1.0, 2.0, 3.0, and 5.0 A g^{-1} are 806, 726, 593, 472, 388, and 287 mA h g^{-1}, respectively. Nanostructuring strategies proposed in this report have a considerable potential in opening new frontiers to high-performance anodes in energy storage systems.

KEYWORDS

electrospinning, hollow metal oxide, Kirkendall effect, lithium-ion batteries, Zeolitic imidazolate frameworks

1 | INTRODUCTION

The development of high-performance Li-ion batteries (LIBs) is pivotal for portable energy storage devices and electric vehicles (EV).[1-3] Transition metal oxides (TMOs) are considered as potential alternatives to the commercial graphite anode owing to their high gravimetric as well as volumetric specific capacities based on the conversion reaction, low price, and abundant resources.[4] However, the practical applications of these TMOs as anodes is limited by the drastic specific volume variations of materials during Li^+ insertion and extraction processes and the relatively low electrical conductivities; this leads to the destruction of anode structures, which results in rapid capacity fading and large cell resistance during cycles.[5,6] The nanostructuring strategy of anode materials can be one of the fundamental approaches to enhance the performance of LIBs for addressing these limitations. Consequently, the anode material designed in a sophisticated manner can accommodate strain during cycles, shorten the pathways for lithium ions and electrons, and highly enhance the electrolyte contact area during cycles.

Recently, hybridization of TMOs with different metal species has proved to be effective to improve the

electrochemical performance of LIBs compared to the use of single metal oxide for anodes.[7-9] In general, the expansion coefficients are different for two different metals.[10] As a result, monometallic oxides, produced in the reaction with Li^+ after the first cycle, serve as a soft matrix to buffer the volume expansion of lithiation/delithiation during cycles. In addition, bimetallic oxides can react with more Li^+ ions compared to single metal oxides because of the complex chemical compositions; this results in higher reversible capacities. Further, bimetallic oxides show higher electrical conductivity compared to monometallic oxides, resulting in lower activation energy for electron transfer between cations for bimetallic analogues.[11] Two members of the TMOs family—Co_3O_4 and Fe_2O_3—are the most extensively studied anode components because of their high abundance, theoretical capacity, nontoxic properties, and also by benefiting from the strategy of the hybridization of TMOs. Thus far, various nanostructures of Co_3O_4 and Fe_2O_3 including nanowires, hollow microcubes, branched nanowires, and nanoneedles have been introduced as anodes in LIBs.[12-15] However, most of these studies have focused on every single Co_3O_4 or Fe_2O_3 based anodes.

In this study, we designed a unique nanofiber structure comprising dual-phase Co_3O_4/Fe_3O_4 hollow nanospheres and nitrogen-doped carbon by applying a nanoscale Kirkendall diffusion mechanism to Zeolitic imidazolate frameworks (ZIFs) in nanofibers obtained by electrospinning as LIBs anodes. The ZIFs, metal ion nodes, and organic linkers containing Metal-Organic Frameworks (MOFs), deliver high porosity, large specific surface area, and structural diversity.[16,17] Among MOFs, ZIF-67 is composed of Co ions as metallic nodes and 2-methylimidazole (2-mIM) as an organic linker. In this study, optimized ZIFs containing both Co and Fe ion nodes can be facile prepared by the supplementation of additional Fe salt in the solution for the ZIF-67 synthesis with Co ion nods. In addition, the size of ZIF polyhedron was controlled by adjusting the trimethylamine content as an additive added in the synthetic solution to prepare composite ZIFs polyhedron efficiently in the fiber structure during the electrospinning process.[18] Hollow-structured dual-phase Co_3O_4/Fe_3O_4 nanospheres in the nanofiber structure can be obtained by application of the Kirkendall diffusion mechanism in nanoscale to the as-spun composite fibers by performing simple heat treatments. These hollow Co_3O_4/Fe_3O_4 nanospheres are expected to provide higher surface area and lithium binding sites leading to short Li^+ ion diffusion path length compared to the solid ones.[19-22] The large volume changes due to cycling can be accommodated by the inner hollow spaces resulting prevention of the self-aggregation of nanostructured subunits, which leads to better capacity retention.[20,21,23] In addition, the nitrogen-doped porous carbon matrix of the structure is beneficial for further improvement in the cell electrical conductivity, penetration of electrolyte, and diffusion of Li^+ ions at the time of cycling.[24] All these factors lead to enhanced lithium storage capability and stability of the cell. We believe that the present strategy of synthesizing unique porous nanofibers comprising dual-phase Co_3O_4/Fe_3O_4 hollow nanospheres and nitrogen-doped carbon can be utilized for developing advanced anode materials for viable LIB technologies.

2 | EXPERIMENTAL

Porous nanofibers comprising dual-phase Co_3O_4/Fe_3O_4 hollow nanospheres and N-doped C were prepared by the electrospinning technique and followed by thermal treatments. To prepare the spinning solution, 0.5 g prepared Fe@ZIF-67 particles and 12 wt% polyacrylonitrile (PAN, MW 150000, Sigma Aldrich) were added to 10 mL N, N-Dimethylformamide (DMF, 99% purity, Samchun) solvent and stirred vigorously overnight. Fe@ZIF-67 particles were prepared in advance by dissolving 32.8 mM of $Co(NO_3)_2{\cdot}6H_2O$ (98% purity, Junsei) and 16.4 mM of $Fe(NO_3)_3{\cdot}9H_2O$ (98% purity, Sigma Aldrich) in 50 mL distilled water. In addition, 396 mM 2-methylimidazole (99% purity, Acros Organics) and 6 mL triethylamine (TEA, 99% purity, Alfa Aesar) were dissolved in another 50 mL distilled water; then, it was poured into the above solution to be mixed homogeneously. After 24 hours, the deep purple solid product (Fe@ZIF-67) was produced by centrifugation. A plastic syringe containing 21-gauge stainless-steel needle was loaded with the spinning solution. The flow rate of solution ejection was controlled at 4 mL h^{-1}; a distance of 15 cm kept between needle tip and collector, applied voltage was 17 kV, and the collector was rotated at 300 rpm. As-spun Fe@ZIF-67/PAN composite fibers heated at 120°C in the air for stabilization. Stabilized fibers were heat-treated at 800°C for 5 hours at a heating rate of 5°C min^{-1} under N_2 atmosphere. Subsequently, it was heat-treated a second time at various temperatures of 200°C, 300°C, 400°C, and 500°C, respectively for 2 hours in air at a heating rate of 5°C min^{-1}. The nanofibers finally obtained after the second heat treatments at 200°C, 300°C, 400°C, and 500°C are designated as "A200NF," "A300NF," "A400NF," and "A500NF" for simplicity.

3 | RESULTS AND DISCUSSIONS

The porous nanofibers comprising of dual-phase Co_3O_4/Fe_3O_4 hollow nanospheres and N-doped C were prepared through the Kirkendall diffusion mechanism in

nanoscale to the as-spun Fe@ZIF-67/PAN composite fibers obtained by electrospinning. The Scheme 1 systematically depicts formation pathways of the unique nanostructures in detail. The as-prepared electrospun fiber precursors composed of Fe-incorporated ZIF-67 polyhedron (Fe@ZIF-67) and PAN are prepared by electrospinning (Scheme 1-①). After the first heat treatment under N_2 atmosphere, the Fe@ZIF-67 polyhedron in the composite are carbothermaly reduced into metallic Co and CoFe solid solution (Scheme 1-②). Concurrently, the PAN matrix is carbonized and subsequently doped with N, which result in a N-doped C matrix surrounding the metallic Co and CoFe nanocrystals (Scheme 1-②). 2-mIM, as an organic linker of Fe@ZIF-67, acts as an N-doping source under N_2 atmosphere.[25,26] Further, during carbothermal reduction, metallic Co and CoFe crystals play the role of catalysts for the graphitization of carbon formed by PAN.[25,26] Thus, carbonization of both the organic linker of Fe@ZIF-67 and PAN into graphitic carbon (GC) doped with N leads to metallic Co and CoFe nanospheres coated with N-doped GC (N-GC) in the structure. After the second heat treatment in an air atmosphere, the filled Co and CoFe metals dispersed within the N-GC matrix are converted into hollow structured Co_3O_4 and Fe_3O_4 nanospheres by the well-known Kirkendall diffusion effect (Scheme 1-③). The detailed Kirkendall diffusion mechanism is displayed in Scheme S1. The formation of nanostructured core-shell metal@-metal oxide particles was resulted from the surface oxidation of the metallic Co and CoFe nanocrystals. The outward diffusion of Co and Fe cations occurred faster than the internal diffusion of air; therefore, the generation of Kirkendall voids at the time of vacancy-assisted material through bulk interdiffusion near the metal@-metal oxide interface; this gives rise to the coarsening and enhancement of pore growth in spheres. Eventually, transformation of metal to metal oxide through the Kirkendall diffusion led to the formation of N-GC layer coated hollow Co_3O_4 and Fe_3O_4 nanospheres.

The formation mechanism of the porous nanofibers comprising dual-phase Co_3O_4/Fe_3O_4 hollow nanospheres and N-GC elucidated more comprehensively through detailed investigation of each heat treatment induced morphological and phase changes in nanofibers. The morphologies of stabilized Fe@ZIF-67/PAN composite fibers at 120°C are displayed in Figure 1. A continuous one-dimensional (1-D) fibrous morphology with a uniform diameter of ~1.5 μm are observed from the FE-SEM images (Figure 1A,B). In addition, the bumpy surface of the nanofiber (Figure 1B) proves the uniform dispersion of the Fe@ZIF-67 polyhedron with an average size of 90 nm in the composite. In this study, the size of Fe@ZIF-67 polyhedron is optimized by adjusting the content of triethylamine (TEA) added in the synthetic solution to disperse it efficiently in the fiber structure during spinning.[18] The Scheme S2 describes the size-control mechanism in Fe@ZIF-67. Fe@ZIF-67 obtained without TEA forms a flat-leaf structure by 2-D networking between transition metal ions (Co^{2+} and Fe^{3+}) and a 2-mIM organic linker.[27] However, an increase in the pH caused by adding TEA induces the acceleration of the nucleation rate of crystals; the crystals follow the growth via heterogeneous nucleation. Therefore, polyhedral-shaped crystals enclosed by (111) crystallographic facets are formed because of (111) planes, which have the lowest surface energy for the face-centered cubic crystal structure. Subsequently, the increasing pH value with more TEA gradually accelerates the nucleation rate, and this results in a decrease in the crystal size.[28] Physical characteristics of FE-SEM and the XRD results of as-prepared Fe@ZIF-67 polyhedron are shown in Figure S1. The Fe@ZIF-67 obtained without TEA shows a flat leaf structure (Figure S1A) caused by 2-D networking between the metal ions and 2-mIM organic linkers. The Fe@ZIF-67 particle obtained from the solution with 3 mL TEA shows a polyhedron structure (Average size: ~250 nm), as indicated in Figure S1B. The TEA increases the pH of the solution as an organic base, and this increases the nucleation rate of Fe@ZIF-67 and changes the structure to a polyhedron. The FE-SEM of the Fe@ZIF-67 obtained from the solution with 6 mL TEA shows a polyhedron structure and has the smallest mean

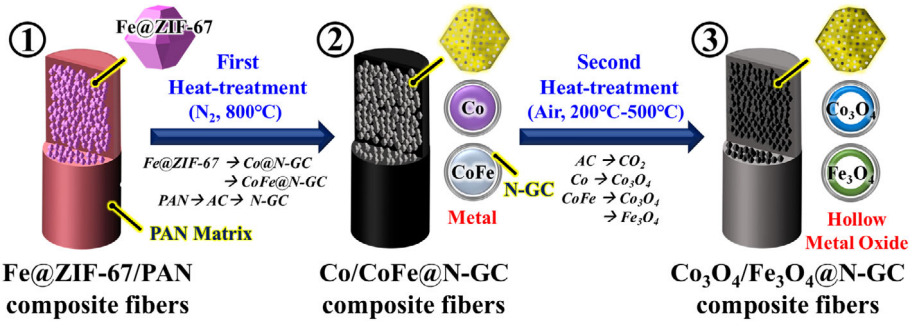

SCHEME 1 Synthetic mechanism of the porous nanofibers comprising dual-phase Co_3O_4/Fe_3O_4 hollow nanospheres and N-doped graphitic carbon

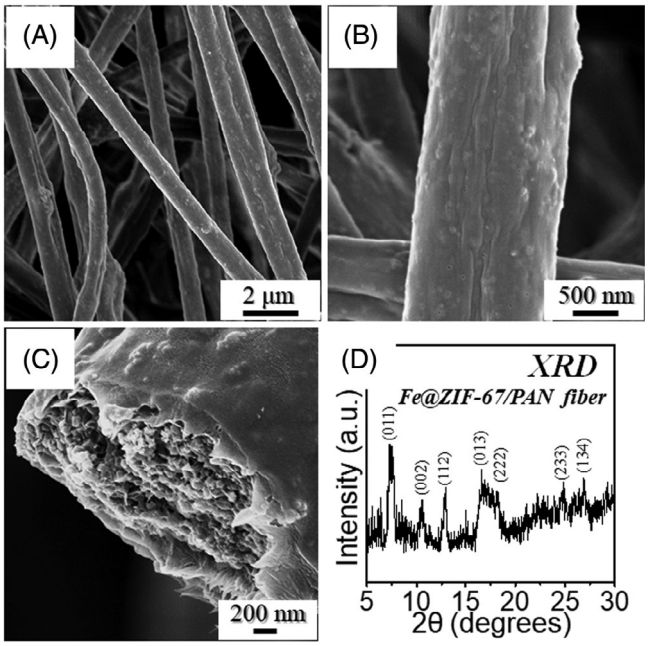

FIGURE 1 (A–C) Morphologies and (D) XRD pattern of the as-spun Fe@ZIF-67/PAN composite fibers after stabilization at 120°C

size of 90 nm, as indicated in Figure S1C. In this study, the Fe@ZIF-67 with a size of 90 nm was selected to be composited effectively in the fiber structure with a mean diameter of 1.5 μm during spinning. The XRD pattern of the selected Fe@ZIF-67 with 90 nm (Figure S1D) was well matched with the previously reported XRD pattern of ZIF-67 without the incorporation of the Fe ion; this indicates that the conformational change of Fe@ZIF-67 did not occur.[29] The detailed morphology of the selected Fe@ZIF-67 with 90 nm is shown in Figure S2. The elemental mapping images (Figure S2E) prove that Fe ions are well incorporated into the ZIF-67 structure. The cross-sectioned FE-SEM image of the fiber proves the good distribution of the optimized Fe@ZIF-67 polyhedron in the fibers (Figure 1C). The image clearly shows that the Fe@ZIF-67 polyhedrons are well confined and sparsely distributed within the fiber framework. The XRD pattern of the Fe@ZIF-67/PAN composite fibers (Figure 1D) primarily display a diffraction pattern of Fe@ZIF-67 polyhedron (Figure S1D) because of the high amount of Fe@ZIF-67 nanocrystals in the PAN matrix.

Nanofibers obtained after the first heat treatment at 800°C are shown in Figure 2. The FE-SEM images (Figure 2A,B) exhibit the well-reserved 1-D fiber structure obtained even after heat treatment. However, the nanofiber shrinks in diameter from 1.5 μm to 250 nm after the heat treatment. In addition, the PAN—a matrix of the composite—was carbonized; concurrently, transition metal ions (Co^{2+} and Fe^{3+}) of the Fe@ZIF-67 polyhedron were reduced into Co and CoFe metallic nanocrystals by carbothermal reduction. Therefore, the homogeneous distribution of ultrafine nanoparticles with a filled structure all over the fiber structure are displayed in Figure 2C. The graphitic carbon (GC) rings formed with the help of Co and Fe catalysts for the graphitization of C matrix are observed around metallic nanoparticles as shown by arrows in Figure 2D. The crystallinity of these carbon materials in the Co/CoFe/N-GC composite nanofibers is analyzed by Raman spectroscopy shown in Figure S3. The degree of crystallinity in carbonaceous materials can be precisely evaluated from the ratio of peak intensity between D (1350 cm^{-1}) and G (1590 cm^{-1}) bands (I_D/I_G). Thus, smaller I_D/I_G ratio indicates higher is degree of ordering in carbon materials.[26,30] The Co/CoFe/N-GC composite nanofibers exhibit I_D/I_G ratio of ~0.96; it demonstrates that the carbon matrix in the composite is ordered, that is, it is graphitic carbon. From the HR-TEM image (Figure 2E), metallic particles are surrounded by the GC layer, and they show the core shell structure. The XRD (Figure S4A) and SAED (Figure 2F) patterns confirm that the metallic Co (JCPDS card No. 15-0806) and CoFe solid solution (JCPDS card No. 49-1568) phases are formed along with the GC (JCPDS card No. 75-1621) matrix. Elemental mapping images (Figure 2G) further showed that metallic Co and alloy CoFe nanocrystals are uniformly dispersed in GC matrixed nanofibers. In addition, the N content was observed because of N doping into the GC matrix. The 2-mIM, as an organic linker of Fe@ZIF-67, acts as a source of N-doping at the time of annealing in N_2.

Co/CoFe/N-GC composite nanofibers were finally heat-treated at different temperatures of 200°C, 300°C, 400°C, and 500°C under an air atmosphere to apply nanoscale Kirkendall diffusion mechanism to the composite. Morphological changes occurring after heat treatment at 200°C are shown in Figure S5. A200NF has a similar structure to the one (Figure 2) before the second heat treatment. The temperature of 200°C is not sufficient to use the Kirkendall diffusion mechanism on the structure. Therefore, the phase conversion of metallic particles into the metal oxides and the removal of carbon in the composite did not occur, as evident from the XRD pattern of A200NF (Figure S4b). The nanoscale Kirkendall diffusion effect works well at a temperature of 300°C. The morphologies of A300NF obtained after heat treatment at 300°C under an air atmosphere are shown in Figure 3. A300NF has a similar nanofiber morphology to those of Co/CoFe/N-GC composite nanofibers (Figure 2) before the second heat treatment and of A200NF (Figure S5). However, TEM images shown in Figure 3C,D exhibit the uniform dispersion of newly formed hollow nanospheres all over the nanofiber

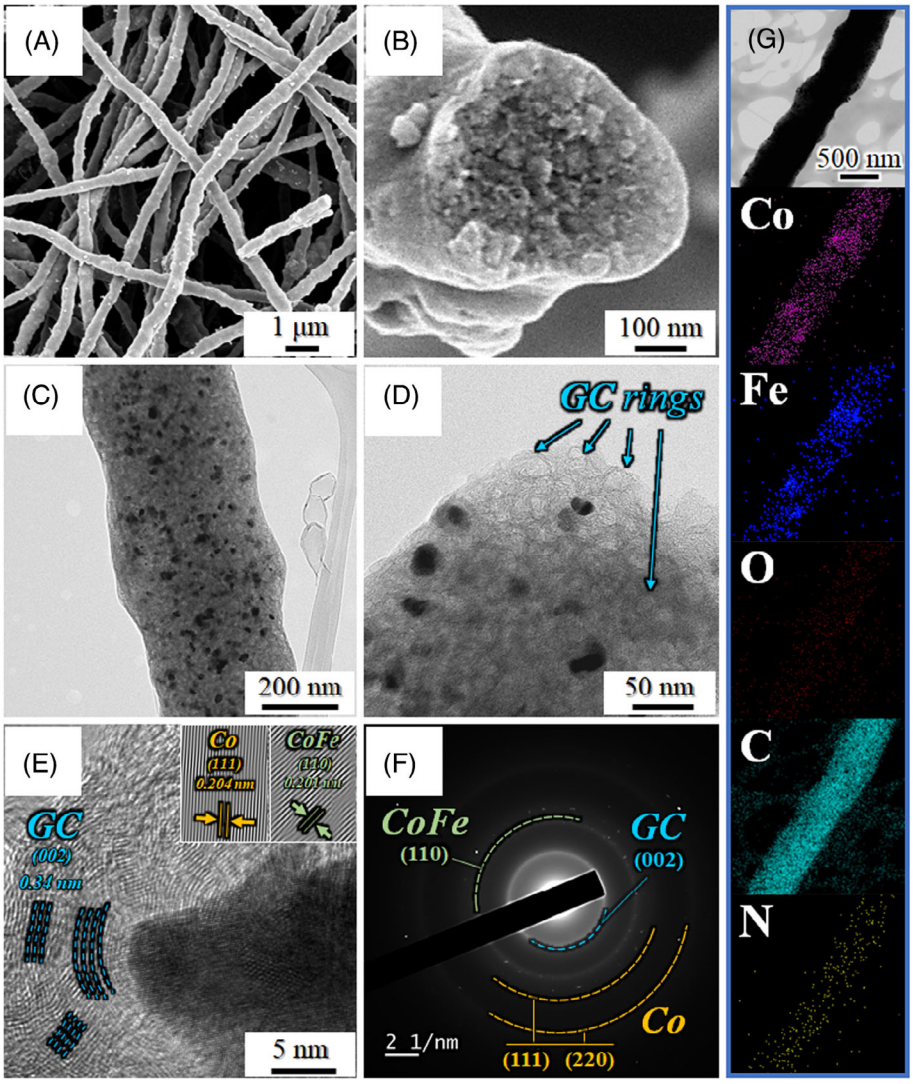

FIGURE 2 Morphologies, SAED pattern, and elemental mapping images of the Co/CoFe/N-GC composite nanofibers obtained after first heat-treatment at 800°C under the N_2 atmosphere: (A, B) FE-SEM images, (C, D) TEM images, (E) HR-TEM image, (F) SAED pattern, and (G) elemental mapping images

structure. The filled-structured metallic Co and CoFe nanoparticles observed before the second heat treatment transformed successfully into hollow-structured Co_3O_4/Fe_3O_4 nanospheres because of the nanoscale Kirkendall diffusion mechanism. The Co (Co^{2+}, 65 pm ; Co^{3+}, 74.5 pm) and Fe (Fe^{2+}, 76 pm; Fe^{3+}, 65 pm) cations with different ionic-radii and diffusion rates in the air atmosphere resulted in dual-phase hollow Co_3O_4/Fe_3O_4 nanospheres. The mean size of hollow nanospheres measured from the HR-TEM image shown in Figure 3D is 28 nm. The HR-TEM image (Figure 3E) shows clear lattice fringes with d-spacing values of 0.244 and 0.209 nm, corresponding to the (311) and (400) crystal planes of Co_3O_4 and Fe_3O_4 phases, respectively. Furthermore, GC with 0.34 nm corresponding to the (002) planes was observed by the surrounding Co_3O_4/Fe_3O_4 nanospheres. The GC component generated by carbothermal reduction during the first heat-treatment process did not combust fully at 300°C. The amount of carbon content in A300NF, as calculated from TGA and the elemental analysis shown in Figure S6, is 44 wt%. The XRD (Figure S4C) and SAED (Figure 3F) patterns of the A300NF further prove the complete conversion of metals into the binary crystal phase of Co_3O_4/Fe_3O_4 after nanoscale Kirkendall diffusion. Elemental mapping images (Figure 3G) unveil the uniform distribution of that hollow Co_3O_4/Fe_3O_4 nanospheres and N doped GC over the A300NF structure.

Chemical states of A300NF were investigated by XPS, as shown in Figure 4A-E and Figure S7. The survey XPS spectrum in Figure S7 shows the presence of Co, Fe, O, C, and N in the composite. The deconvoluted Co 2p XPS spectrum in Figure 4A shows the Co^{3+} peaks of 780.5 eV (Co $2p_{3/2}$) and 795.9 eV (Co $2p_{1/2}$) with two shakeup satellites (denoted as "Sat.") at 787 eV and 803 eV. Additional peaks at 783 eV and 798.3 eV for Co^{2+} are also detected; these peaks correspond to the Co_3O_4 phase.[31,32] The Fe 2p XPS spectrum (Figure 4B) shows peaks at 713.3 eV (Fe $2p_{3/2}$), 725 eV (Fe $2p_{1/2}$), and a shakeup satellite at 718.6 eV. The Fe^{2+} bands at 710.9 eV and 723 eV are

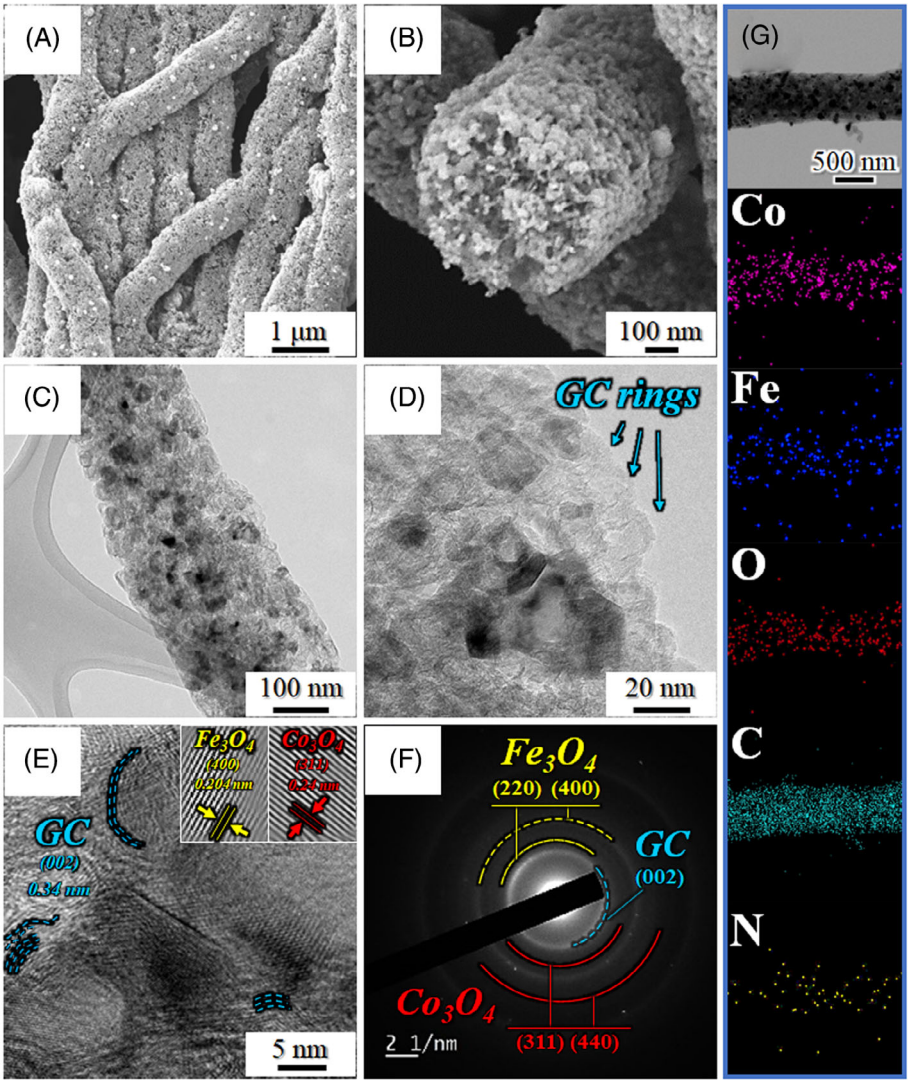

FIGURE 3 Morphologies, SAED pattern, and elemental mapping images of A300NF obtained after second heat-treatment of Co/CoFe/N-GC composite nanofibers at 300°C: (A, B) FE-SEM images, (C, D) TEM images, (E) HR-TEM image, (F) SAED pattern, and (G) elemental mapping images

detected because of the presence of a Fe_3O_4 phase in the structure.[33,34] The metal-oxygen peaks appear at 530.8 eV in the O 1s spectrum, as shown in Figure 4C. The additional peaks at binding energy of 532.7 and 534.3 eV are attributed to the absorbed H_2O on the sample.[35,36] The C 1s XPS spectrum shown in Figure 4D presents the sp^2-bonded carbon (C═C) peak at 284.2 eV, C—N and C—C peaks at 285.1 eV, and C═O peak at 288 eV.[37,38] The presence of graphitic carbon in A300NF is confirmed by the highest intensity of C—C peak among those peaks (Figure 4D). In the N 1s XPS spectrum (Figure 4E), the pyrrolic-N at 400 eV, graphitic-N at 400.9 eV, and oxidized-N species at 401.9 eV are detected.[26,39] These peaks confirm N-doping into carbon. Raman spectroscopy is analyzed as shown in Figure 4F to confirm the crystallinity of the carbon material of A300NF. Compared to the Co/CoFe/N-GC carbon composite with the I_D/I_G ratio of 0.96, it was slightly increased to 0.98, and therefore, A300NF preserved the ordered C matrix even after heating at 300°C in air atmosphere.

The morphologies of nanofibers after the second thermal treatment at 400°C are confirmed as displayed in Figure S8. A400NF reveals morphologies similar to those of the A300NF, as shown in Figure S8A,B. However, the TEM images (Figure S8C,D) indicate that hollow nanospheres observed in A300NF are transformed into a filled structure as a result of sintering at an elevated temperature of 400°C. The TMOs of the filled structures and the GC rings are indicated by the yellow and blue arrows in Figure S8D. The HR-TEM image (Figure S8E) reveals lattice fringes with an equal interplanar distance of 0.244 nm of (311) crystal planes and 0.209 nm of (400) crystal planes for filled structured Co_3O_4 and Fe_3O_4 phases, respectively. XRD (Figure S4D) and SAED (Figure S8F) patterns are in good accordance with the crystal phases of Co_3O_4 and Fe_3O_4. Nanostructure obtained after heat treatment at 500°C is further investigated as shown in Figure S9 to prove the relationship between the fiber morphology and heat-treatment temperature. The overall fiber structure is maintained as

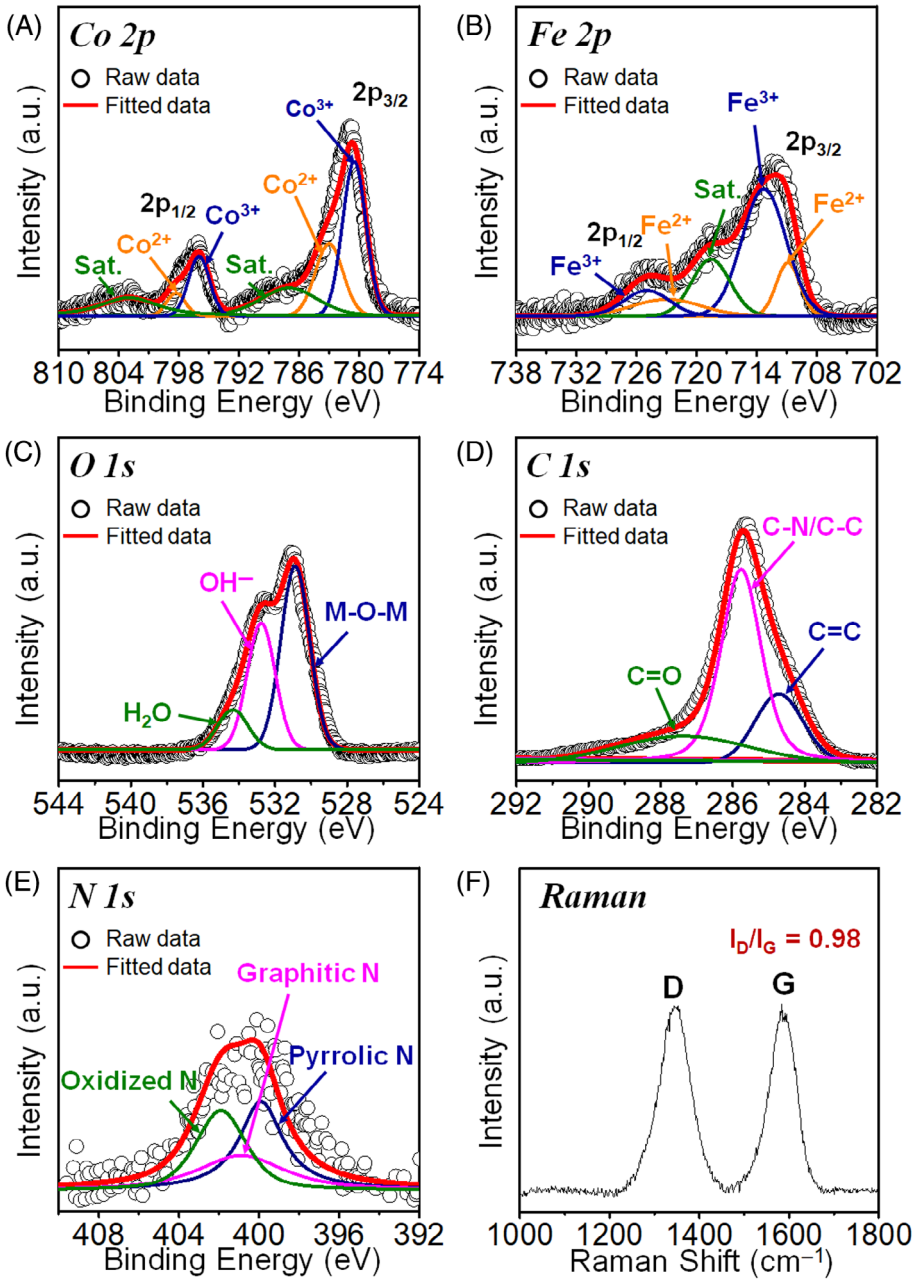

FIGURE 4 Characterization of A300 NF obtained after second heat-treatment at 300°C: (A) Co 2p XPS spectrum, (B) Fe 2p XPS spectrum, (C) O 1s XPS spectrum, (D) C 1s XPS spectrum, (E) N 1s XPS spectrum, and (F) Raman spectrum

shown in Figure S9A,B. However, Co_3O_4 and Fe_3O_4 nanospheres comprising the fiber structure are sintered and densified, and they are grown to large particles with a mean size of 43 nm. The mean crystallite size of nanostructures post-treated at 500°C was calculated to be 42 nm according to the Scherrer's equation considering (311) plane of Fe_3O_4; the average crystallite size is the largest among samples of A200NF (7 nm), A300NF (21 nm), and A400NF (32 nm). The carbon matrix surrounding the Co_3O_4 and Fe_3O_4 nanospheres was not observed owing to the total combustion of C at a high temperature of 500°C. Further, the TG curve proves that there is no C material in A500NF (Figure S6).

The A200NF and A300NF samples show type IV BET adsorption/desorption isotherms with H3 hysteresis, demonstrating their exclusive mesoporous features (Figure S10).[40] BET surface areas of A200NF, A300NF, A400NF, and A500NF are measured to be 180, 152, 40, and 24 $m^2\ g^{-1}$, respectively, as indicated in Figure S10. Notably, the high specific surface area value (A200NF or A300NF sample) of the composites at relatively low oxidation temperatures of 200°C and 300°C is attributed to the formation of unique porous nanofibers comprising of dual-phase hollow nano-sized metal or metal oxide particles and N-doped graphitic C matrix with abundant mesopores. In addition, the A200NF and A300NF show a slight hysteresis loop before 0.5 P/P_o,

indicating a higher degree of open porous structure than the A400NF and A500NF samples. The heat-treatment at higher temperature (400°C and 500°C) results in a significant reduction in the surface area value due to the crystal-growth and sintering of the sample. Accordingly, A500NF showed the lowest specific surface area. The Barrett-Joyner-Halenda pore size distributions is shown in Figure S11. The average pore sizes of the A200NF and A300NF samples were measured as 3.8 and 7.9 nm, respectively. In contrast, the BJH pore-size distribution plots suggest the presence of meso and macro pores in the A400NF and A500NF samples, corroborating with BET isotherms. The BET isotherm and BJH pore size distribution profiles of A200NF and A300NF show uniform pore-size distribution with exceptional mesoporous features than those of A400NF and A500NF samples. Such exclusive mesoporosity and high specific surface area are beneficial in terms of shortening the charge transport paths as they permit the free movement of electrolyte ions into electrode materials.

The Figure 5 shows electrochemical energy storage activities of A200NF, A300NF, A400NF, and A500NF as LIB anodes. The CV curves (scan rate: 0.1 mV s^{-1}) of A300NF for the initial five cycles carried out in 0.001 to 3.0 V vs Li^+/Li (Figure 5A). The irreversible reduction was confirmed by the appearance of peaks at 1.57 and 0.61 V in the first cathodic sweep. The peak at 1.57 V was attributed to the partial insertion of Li^+ ions into the Co_3O_4 and Fe_3O_4 crystals of A300NF by the reactions $Fe_3O_4 + xLi^+ + xe^- \rightarrow Li_xFe_3O_4$ and $Co_3O_4 + xLi^+ + xe^- \rightarrow Li_xCo_3O_4$, respectively. The main peak at 0.61 V could be assigned to the conversion of $Li_xCo_3O_4$ and $Li_xFe_3O_4$ to metallic Co and Fe accompanying the amorphous Li_2O formation and the solid electrolyte interphase (SEI).[41,42] The additional broad peak as a sloping tail below 0.1 V indicates Li^+-intercalation into the N-GC matrix of A300NF. The first anodic peak at 0.24 V is ascribed to the de-intercalation of Li^+ ions from the N-GC matrix.[43] The subsequent peaks at 1.58 and 2.1 V are attributed to the re-combination of each metallic Co and Fe nanograin with oxygen.[26,41] From the second cycle during cathodic scan, peaks shifting to higher potentials at 0.83 and 1.43 V could be assigned to the emergence of ultrafine nanocrystals at the time of Li-ion insertion and desertion during the initial cycle.[44,45] The reversible nature of the electrochemical reactions in A300NF during the cycles was confirmed from the almost identical CV curves of the second cycle. The CV curves of both A400NF and A500NF (Figure S12B,C) are like those of A300NF. However, the peak with a sloping tail below

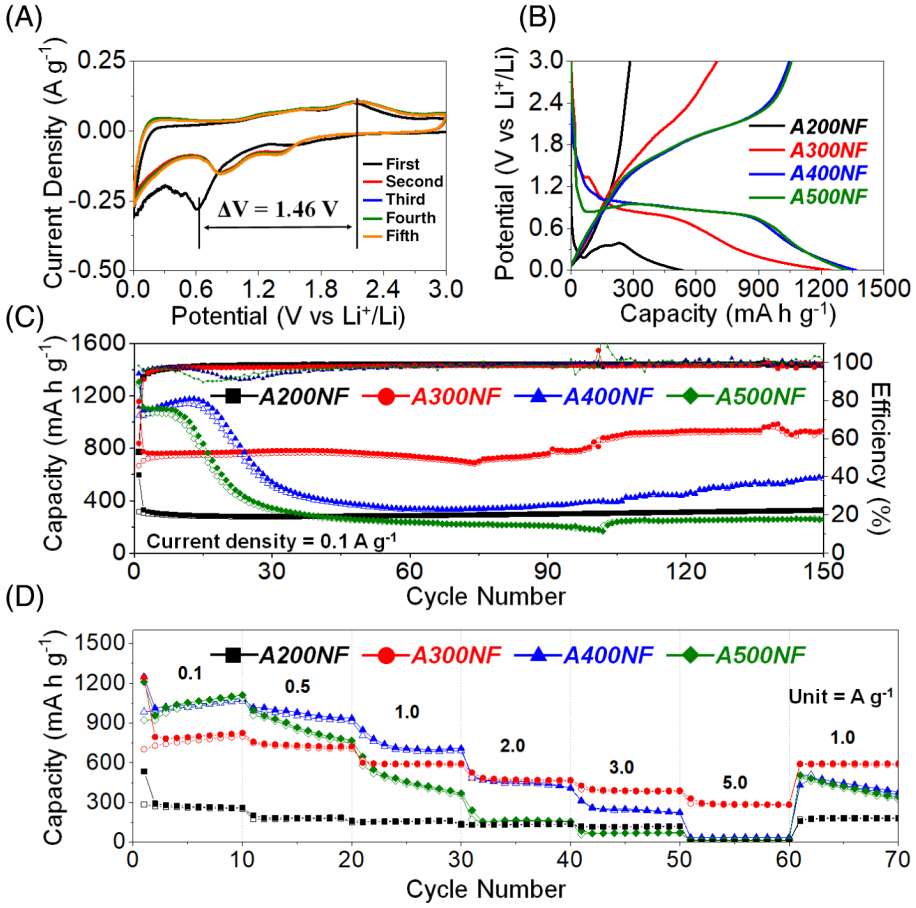

FIGURE 5 Electrochemical properties of the A200NF, A300NF, A400NF, and A500NF: (A) CV curves of A300NF, (B) initial discharge/charge curves at a current density of 0.1 A g^{-1}, (C) cycle performances at a current density of 0.1 A g^{-1}, and (D) rate performances

0.1 V is not observed in A500NF because C is lacking in the structure as a result of the C decomposition at the high temperature (500°C). In addition, A500NF showed that the cathodic peak shifted to the lower potential of 0.31 V because of polarization. This can be attributed to the high-crystallite size of metal oxides without C in A500NF, which hampers the diffusion of both Li^+ ions and electrons during the cycle. In contrast, A300NF showed the smallest polarization potential (ΔV: 0.146 V) compared with A400NF (ΔV: 1.51 V) and A500NF (ΔV: 1.78 V), which suggests that A300NF is a potential candidate as superior anode material among the samples. Hollow dual-phase metal oxides coated with an N-GC layer and a N-GC ring matrix with high electrical conductivity constituting the A300NF can reduce the polarization potential of the sample. This can facilitate better ionic and electron conduction of A300NF. In the case of A200NF (Figure S12A), it is difficult to distinguish the reaction peaks of active materials except for those of carbon because A200NF has metallic Co and Fe phases, which are not converted to their oxide phases. Only peaks at 0.1 V during the reduction and 0.2 V in the anodic process are attributed to the Li^+ insertion and extraction into the C matrix.[43] According to previous reports regarding Co_3O_4 and Fe_3O_4 anodes for LIBs, the discharge and charge process can be summarized by the following Eqs.[41,42,46]

Discharge process:

$$Co_3O_4 + 2Li^+ + 2e^- \rightarrow Li_2Co_3O_4, \quad (1)$$

$$Li_2Co_3O_4 + 6Li^+ + 6e^- \rightarrow 3Co + 4Li_2O, \quad (2)$$

$$Fe_3O_4 + 2Li^+ + 2e^- \rightarrow Li_2Fe_3O_4, \quad (3)$$

$$Li_2Fe_3O_4 + 6Li^+ + 6e^- \rightarrow 3Fe + 4Li_2O. \quad (4)$$

Charge process:

$$3Co + 4Li_2O \rightarrow Co_3O_4 + 8Li^+ + 8e^-, \quad (5)$$

$$3Fe + 4Li_2O \rightarrow Fe_3O_4 + 8Li^+ + 8e^-. \quad (6)$$

The first galvanostatic discharge and charge curves of A200NF, A300NF, A400NF, and A500NF at 0.1 A g^{-1} constant current density are displayed in Figure 5B. The reduction of oxides species was indicated by the sloppy discharge plateau at 0.6 V in A300NF, which is in good agreement with the CV curve (Figure 5A). The charge plateau at 2.1 V is designated to the oxidation of reduced metal nanoparticles in the composite. The initial discharge capacities of the A200NF, A300NF, A400NF, and A500NF were 535, 1245, 1369, and 1331 mA h g^{-1}, respectively. The corresponding Coulombic efficiencies (CE) were 53, 57, 76, and 79%, respectively. The relatively lower CE of A300NF along with A200F compared to A400NF and A500NF could be assigned to the presence of C in large amount with the high initial loss of irreversible capacity in the structure. However, the pre-lithiation of the electrode material can help efficiently reduce the degree of irreversibility during the first cycle.[47] The Figure 5C exhibits the cycling stabilities of nanofibers at 0.1 A g^{-1}. A300NF showed excellent cycling performance with a high reversible discharge capacity of 923 mA h g^{-1} at the 150th cycle. The stable cycling performance of A300NF is achieved by the unique 1-dimensional nanostructure of A300NF. The enhanced capacity retention could be attributed to the effective accommodation of extreme volume changes caused by cycling and also the prevention of self-aggregation of the nanosized fragments by the hollow Co_3O_4 and Fe_3O_4. Further, the N-GC matrix effectively buffers the volume change in the active metal oxide nanostructures caused by surrounding these during the fast charging-discharging process. The discharge capacities of decreased rapidly to 569 and 257 mA h g^{-1} at the 150th cycle in A400NF and A500NF, respectively. The filled metal oxides with a low C content in A400NF and large-sized metal oxides without any C in A500NF would be unable to counter the large strain caused by the volume changes in active materials. This resulted in the agglomeration of nanofibers and pulverization of the electrode during the cycles. Co_3O_4 and Fe_3O_4 crystals of A300NF were etched selectively by the acid treatment of A300NF with hydrochloric acid to determine the capacity contribution of N-GC content in A300NF; this was followed by pure N-GC fibers shown in Figure S13A. The complete removal of Co_3O_4 and Fe_3O_4 phases is confirmed by the EDS spectrum (Figure S13B). Pure N-GC nanofibers demonstrated a reversible discharge capacity of 279 mA h g^{-1} at 0.1 A g^{-1} current density at the 10th cycle (Figure S13C). Therefore, estimated contribution of N-GC matrix to the discharge capacity of A300NF was found to be 30%.

On successive increment in the current density from 0.1 to 5.0 A g^{-1}, the rate performances of A200NF, A300NF, A400NF, and A500NF are as shown in Figure 5D. A400NF and A500NF exhibited higher discharge capacities compared to the other prepared samples at lower current densities below 2.0 A g^{-1}. However, A400NF and A500NF showed rapid deterioration in the discharge capacities to almost zero at 5.0 A g^{-1}. The A400NF/A500NF samples showed final discharge capacities of 1084/1110, 935/767, 706/369, 409/157, 226/71, and 36/12 mA h g^{-1} at 0.1, 0.5, 1.0, 2.0, 3.0, and 5.0 A g^{-1}

current densities, respectively. In contrast, A300NF showed stable discharge capacities, even at high current densities till 5.0 A g^{-1}. Final discharge capacities of A300NF at current densities of 0.1, 0.5, 1.0, 2.0, 3.0, and 5.0 A g^{-1} were 806, 726, 593, 472, 388, and 287 mA h g^{-1}, respectively. Further, A300NF exhibited good recovery in the discharge capacity of 589 mA h g^{-1} on returning to 1.0 A g^{-1} after cycling at higher current densities, which indicates its high structural stability. A better rate property of A300NF can be achieved in this study by the synergetic effects of the unique nanostructure of A300NF. To confirm the synergistic effect of Fe_3O_4 and Co_3O_4, the porous nanofibers comprising of N-doped carbon and ZIF-67-derived single-phase Co_3O_4 hollow nanospheres (without adding Fe salts) were prepared (Figure S14A-C). The prepared Co_3O_4 single-phase nanofibers exhibited a very low discharge capacity of 13 mA h g^{-1} at a high current density of 5.0 A g^{-1} and poor stability than dual-phase A300NF (Figure S14D). The presence of hollow Co_3O_4 and Fe_3O_4 nanospheres in A300NF provided a higher surface area and accessible sites for lithium storage, which can significantly shorten the diffusion path length of Li^+ ions compared to the solid ones. Moreover, N-GC layer covered on the metal oxides and N doped porous carbon matrix led to the enhanced electrical conductivity, better penetration of electrolyte, and diffusion of Li^+ ions during cycling. These factors give rise to the enhanced rate property of A300NF.

The kinetics of electrochemical reactions in the cell are studied via cyclic voltammetry between 0.001 and 3.0 V at various scan rates of 0.2-1.5 mV to elucidate the excellent rate capability of A300NF, as shown in Figure 6A. Furthermore, the redox peak currents (i) measured from the CV curves at different scan rates (v) are analyzed to differentiate between capacitive and diffusion-controlled processes according to

$$i = av^b, \tag{7}$$

$$\log(i) = b\log(v) + \log(a), \tag{8}$$

where a and b represent adjustable parameters.[48,49] The electrochemical reaction process is dominated by diffusion-controlled behaviors when the value of b is ~0.5. It is dominated by capacitive-controlled behaviors if b converges to 1.0.[50,51] The values of b for different cathodic and anodic peaks are calculated from the slope of $\log(i)$ vs $\log(v)$ plots.[26] The b values for peaks 1, 2, 3, and 4 (Figure 6B) of A300NF are 0.85, 0.88, 0.95, and 0.89, respectively. These values are close to 1.0, which suggests a dominant capacitive-controlled redox kinetics for A300NF. In contrast, A400NF and A500NF (Figure S15B,F) show lower b values, which indicates that they dominate the diffusion-controlled behavior during the electrochemical reaction process. In general, the reaction kinetics is closely dependent to the capacitive effect of the electrode material; this implies that, higher percentage of capacitive-controlled process would be beneficial for better transport kinetics and thereby enhancing

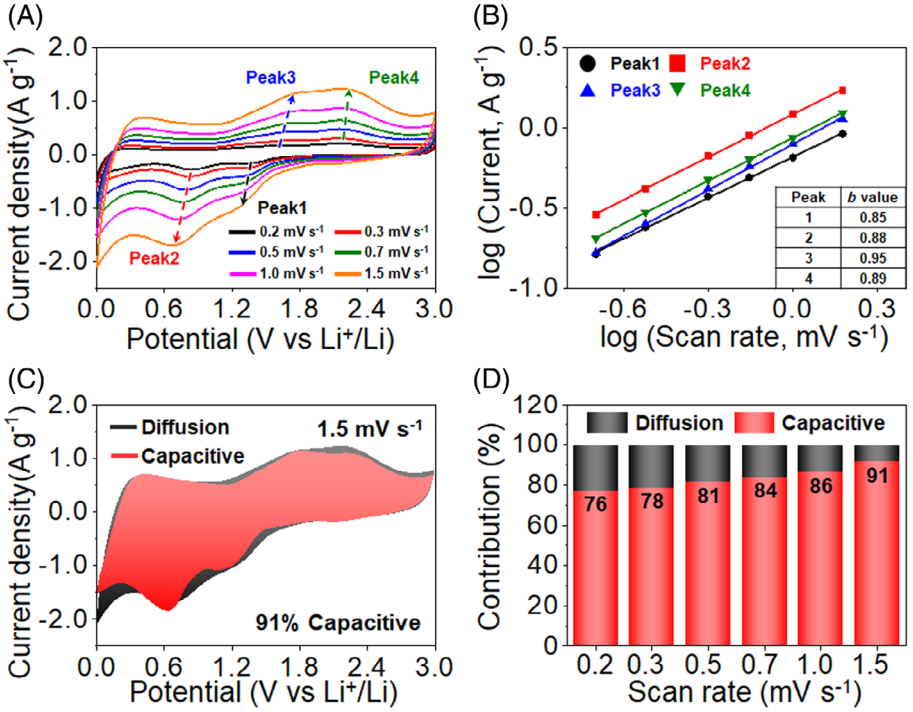

FIGURE 6 Electrochemical reaction dynamics analysis of A300NF: (A) CV curves at different scan rates, (B) plot between $\log(i)$ vs $\log(v)$ for each redox peak, (C) CV curve with the capacitive proportion by the red region at 1.5 mV s^{-1}, and (D) bar chart exhibiting the capacitive fraction at various scan rates

the rate-performance of the cells.[26] The total charge accumulated at the electrode material could be divided into a capacitive and diffusion-limited process for a quantitative analysis of the capacitive contribution using

$$i = k_1 v + k_2 v^{1/2}, \quad (9)$$

where $k_1 v$ and $k_2 v^{1/2}$ represent the contribution from the capacitive and diffusion-controlled process, respectively.[50,52] The Figure 6C shows ~91% capacitive contribution, which is consistent with the high *b*-values close to 1.0 in Figure 6B. Capacity contributions of A400NF and A500NF (Figure S15C,G) are calculated as 74% and 70%, respectively, which is lower than those of A300NF. The capacitive contribution of A300NF is calculated at different scan rates as shown in Figure 6D. A300NF exhibits capacitive contributions of 76%, 78%, 81%, 84%, 86%, and 91% at scan rates of 0.2, 0.3, 0.5, 0.7, 1.0, and 1.5 mV s^{-1}, respectively. The capacitive contribution of A400NF (Figure S15D) is calculated as 45%, 47%, 52%, 56%, 64%, and 74%, and that of A500NF (Figure S15H) is calculated as 39%, 42%, 46%, 51%, 59%, and 70%, respectively. As expected, compared to A300NF, the other nanofibers deliver a lower capacitive contribution, which can be explained by the relatively low *b* values. The fast transport of Li^+ ions is indicated by the high proportion of the capacitive controlled contribution of A300NF, which improves the rate performance and cycle stability of the cell. Hollow Co_3O_4 and Fe_3O_4 nanospheres constituting A300NF provide higher surface areas and lithium binding sites, and they shorten the Li^+ ion diffusion path length. Moreover, enhanced the electrical conductivity of the cell, electrolyte penetration, and diffusion of Li^+ ion during cycling were achieved by the presence of N-GC layer covered on the metal oxides and N-doped porous carbon matrix.

The superior Li^+ storage activity of A300NF is further supported by the electrochemical impedance spectroscopy (EIS) analyses before and after 1, 100, and 150 cycles in the fully charged state, which is fitted with a Randle-type equivalent-circuit model (Figure S16A,B) shown in Figure 7. The semicircles observed at the medium-frequency range in Nyquist plots indicate the charge-transfer resistance (R_{ct}) of electrodes.[53] The R_{ct} values of samples were 1650, 399, 288, and 203 Ω for A200NF, A300NF, A400NF, and A500NF, respectively, before cycling (Figure 7A). The R_{ct} values of the samples decreased to 42 Ω for A300NF, 41 Ω for A400NF, and 42 Ω for A500NF after the first cycle because of the

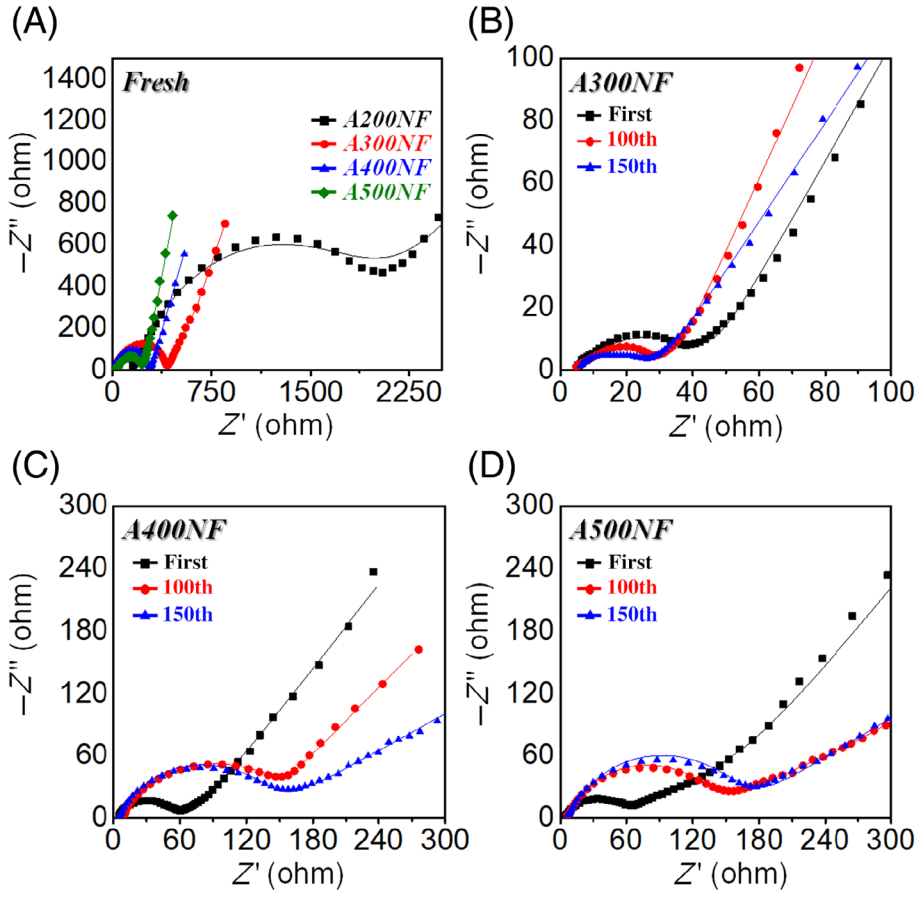

FIGURE 7 Nyquist impedance plots of the Co_3O_4/Fe_3O_4@N-GC composite nanofibers: (A) before cycling and after first, 100th, and 150th cycle of (B) A300NF, (C) A400NF, and (D) A500NF

emergence of ultrafine nanocrystals during the initial cycle, as shown in Figure 7A-C. The R_{ct} values of A300NF decreased to 30 Ω after 100 cycles and were almost maintained till 150 cycles, as shown in Figure 7B. The R_{ct} values of A400NF and A500NF increased to 129 Ω and 143 Ω after 150 cycles (Figure 7C,D); this is because of the structural destruction of Co_3O_4 and Fe_3O_4 with the filled structure by the repeated lithiation/de-lithiation processes. Therefore, the high electrical conductivity and structure stability of A300NF during the repeated lithiation and de-lithiation processes could be established from the findings of the EIS analysis. The hollow Co_3O_4 and Fe_3O_4 coated with N-GC layer and N doped C matrix improve the electrical conductivity as well as structural stability of A300NF. Furthermore, the FE-SEM and TEM images of all samples after 100 cycles were captured to realize their structural integrity and durability, as shown in Figure S8. The resultant images indicate that A200NF and A300NF maintain their original nanofiber structure without any significant structural collapse, even after repeated lithiation/de-lithiation for 100 cycles (Figure 8A,B). However, A400NF and A500NF (Figure 8C,D) cannot withstand the internal stress caused by the volume variation, and therefore, the nanofiber structure is fragmented into several pieces after cycling. Based on these results, the hollow hybrid oxide

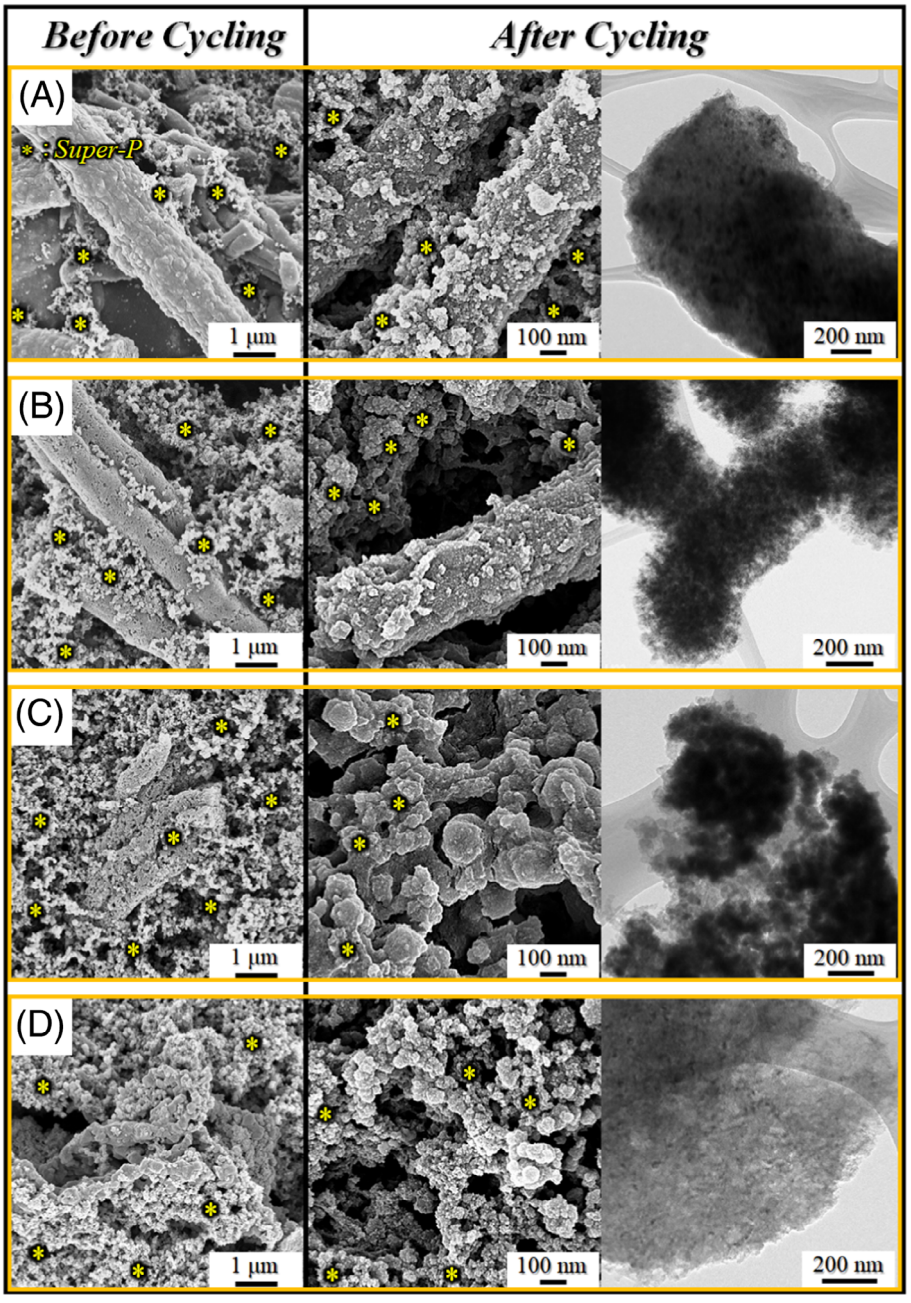

FIGURE 8 Morphologies of the (A) A200NF, (B) A300NF, (C) A400NF, and (D) A500NF obtained before cycling and after 100 cycling

nanospheres covered with N-GC relieved volume expansion during cycling, provided a short diffusion path for lithium ions and a large specific surface area, which allows the liquid electrolyte to penetrate efficiently. The above strategies applied to A300NF improved its overall electrochemical performance.

4 | CONCLUSIONS

Porous nanofibers comprising dual-phase Co_3O_4/Fe_3O_4 hollow nanospheres and N-doped graphitic C matrix were fabricated through electrospinning and multi-step heat treatments. The size of Fe@ZIF-67 was controlled by adjusting the pH of the solution. The Fe@ZIF-67 crystals with an average size of 90 nm could be well distributed in the as-spun PAN fiber structure. The dual-phase Co_3O_4/Fe_3O_4 hollow nanospheres generated via the Kirkendall diffusion mechanism provide the fast diffusion of Li^+ ions compared to a filled structure. In addition, effective accommodation of the large volume changes upon cycling and prevention of self-aggregation of the nanosized subunits resulted the improved electrochemical performance. The N-doped porous carbon matrix improves the electrical conductivity of the cell and achieved better electrolyte penetration as well as Li^+ ion diffusion during cycling. All these factors afford superior lithium storage capability and stability of the cell. We believe that the proposed strategy of synthesizing unique porous nanofiber comprising dual-phase Co_3O_4/Fe_3O_4 hollow nanospheres and N-doped C can be utilized for the development of advanced anode materials for viable LIBs technology.

ACKNOWLEDGEMENT

This research was supported by Chungbuk National University Korea National University Development Project (2021).

DATA AVAILABILITY STATEMENT

The author elects to not share data Research data are not shared.

ORCID

Jung Sang Cho https://orcid.org/0000-0001-5584-1526

REFERENCES

1. He C, Wu S, Zhao N, Shi C, Liu E, Li J. Carbon-encapsulated Fe_3O_4 nanoparticles as a high-rate lithium ion battery anode material. *ACS Nano*. 2013;7(5):4459-4469.
2. Peng C, Chen B, Qin Y, et al. Facile ultrasonic synthesis of CoO quantum dot/graphene nanosheet composites with high lithium storage capacity. *ACS Nano*. 2012;6(2):1074-1081.
3. Mai L, Xu L, Han C, et al. Electrospun ultralong hierarchical vanadium oxide nanowires with high performance for lithium ion batteries. *Nano Lett*. 2010;10(11):4750-4755.
4. Rai AK, Gim J, Thi TV, Ahn D, Cho SJ, Kim J. High rate capability and long cycle stability of $Co_3O_4/CoFe_2O_4$ nanocomposite as an anode material for high-performance secondary lithium ion batteries. *J Phys Chem C*. 2014;118(21):11234-11243.
5. Nie Y, Wang F, Zhang H, et al. Tunable confinement of Cu-Zn bimetallic oxides in carbon nanofiber networks by thermal diffusion for lithium-ion battery. *Appl Surf Sci*. 2020;517:146079.
6. Li Y, Song Y, Wang H, et al. Electrospinning-based construction of porous Mn_3O_4/CNFs as anodes for high-performance lithium-ion batteries. *New J Chem*. 2020;44(10):3888-3895.
7. Xiong QQ, Tu JP, Xia XH, Zhao XY, Gu CD, Wang XL. A three-dimensional hierarchical Fe_2O_3@NiO core/shell nanorod array on carbon cloth: a new class of anode for high-performance lithium-ion batteries. *Nanoscale*. 2013;5(17):7906-7912.
8. Hou Q, Man Q, Liu P, et al. Encapsulation of Fe_2O_3/NiO and Fe_2O_3/Co_3O_4 nanosheets into conductive polypyrrole for superior lithium ion storage. *Electrochim Acta*. 2019;296:438-449.
9. Zhang SL, Guan BY, Wu HB, Lou XW. Metal–organic framework-assisted synthesis of compact Fe_2O_3 nanotubes in Co_3O_4 host with enhanced lithium storage properties. *Nanomicro Lett*. 2018;10(3):1-9.
10. Zhao Y, Li X, Yan B, et al. Recent developments and understanding of novel mixed transition-metal oxides as anodes in lithium ion batteries. *Adv Energy Mater*. 2016;6(8):1502175.
11. Yuan C, Wu HB, Xie Y, Lou XW. Mixed transition-metal oxides: design, synthesis, and energy-related applications. *Angew Chem Int Ed*. 2014;53(6):1488-1504.
12. Xiong QQ, Xia XH, Tu JP, et al. Hierarchical Fe_2O_3@Co_3O_4 nanowire array anode for high-performance lithium-ion batteries. *J Power Sources*. 2013;240:344-350.
13. Li Z, Li B, Yin L, Qi Y. Prussion blue-supported annealing chemical reaction route synthesized double-shelled Fe_2O_3/Co_3O_4 hollow microcubes as anode materials for lithium-ion battery. *ACS Appl Mater Interfaces*. 2014;6(11):8098-8107.
14. Wu H, Xu M, Wang Y, Zheng G. Branched Co_3O_4/Fe_2O_3 nanowires as high capacity lithium-ion battery anodes. *Nano Res*. 2013;6(3):167-173.
15. Luo Y, Kong D, Luo J, et al. Seed-assisted synthesis of Co_3O_4@α-Fe_2O_3 core-shell nanoneedle arrays for lithium-ion battery anode with high capacity. *RSC Adv*. 2014;4(26):13241-13249.
16. Wang C, Kaneti YV, Bando Y, et al. Metal–organic framework-derived one-dimensional porous or hollow carbon-based nanofibers for energy storage and conversion. *Mater Horiz*. 2018;5(3):394-407.
17. Guan BY, Yu XY, Wu HB, Lou XW. Complex nanostructures from materials based on metal–organic frameworks for electrochemical energy storage and conversion. *Adv Mater*. 2017;29(47):1703614.
18. Zhao Y, Zhang Q, Li Y, Zhang R, Lu G. Large-scale synthesis of monodisperse UiO-66 crystals with tunable sizes and missing linker defects via acid/base co-modulation. *ACS Appl Mater Interfaces*. 2017;9(17):15079-15085.
19. Park GD, Cho JS, Kang YC. Multiphase and double-layer $NiFe_2O_4$@NiO-hollow-nanosphere-decorated reduced graphene

oxide composite powders prepared by spray pyrolysis applying nanoscale Kirkendall diffusion. *ACS Appl Mater Interfaces*. 2015;7(30):16842-16849.
20. Koo B, Xiong H, Slater MD, et al. Hollow iron oxide nanoparticles for application in lithium ion batteries. *Nano Lett*. 2012;12(5):2429-2435.
21. Guo H, Li T, Chen W, et al. General design of hollow porous $CoFe_2O_4$ nanocubes from metal–organic frameworks with extraordinary lithium storage. *Nanoscale*. 2014;6(24):15168-15174.
22. Cho JS, Hong YJ, Kang YC. Design and synthesis of bubble-nanorod-structured Fe_2O_3–carbon nanofibers as advanced anode material for Li-ion batteries. *ACS Nano*. 2015;9(4):4026-4035.
23. Cho JS, Lee JK, Kang YC. Graphitic carbon-coated $FeSe_2$ hollow nanosphere-decorated reduced graphene oxide hybrid nanofibers as an efficient anode material for sodium ion batteries. *Sci Rep*. 2016;6(1):1-13.
24. Jeong SY, Ghosh S, Kim JK, et al. Multi-channel-contained few-layered $MoSe_2$ nanosheet/N-doped carbon hybrid nanofibers prepared using diethylenetriamine as anodes for high-performance sodium-ion batteries. *J Ind Eng Chem*. 2019;75:100-107.
25. Yang SH, Park SK, Kim JK, Kang YC. A MOF-mediated strategy for constructing human backbone-like $CoMoS_3$@ N-doped carbon nanostructures with multiple voids as a superior anode for sodium-ion batteries. *J Mater Chem A*. 2019;7(22):13751-13761.
26. Lee JS, Jo MS, Saroha R, et al. Hierarchically well-developed porous graphene nanofibers comprising N-doped graphitic C-coated cobalt oxide hollow nanospheres as anodes for high-rate Li-ion batteries. *Small*. 2020;16(32):2002213.
27. Jang JS, Koo WT, Kim DH, Kim ID. In situ coupling of multi-dimensional MOFs for heterogeneous metal-oxide architectures: toward sensitive chemiresistors. *ACS Cent Sci*. 2018;4(7):929-937.
28. Wang F, Guo H, Chai Y, Li Y, Liu C. The controlled regulation of morphology and size of HKUST-1 by "coordination modulation method". *Microporous Mesoporous Mater*. 2013;173:181-188.
29. Park SK, Kang YC. MOF-templated N-doped carbon-coated $CoSe_2$ nanorods supported on porous CNT microspheres with excellent sodium-ion storage and electrocatalytic properties. *ACS Appl Mater Interfaces*. 2018;10(20):17203-17213.
30. Qi Y, Zhang H, Du N, Yang D. Highly loaded CoO/graphene nanocomposites as lithium-ion anodes with superior reversible capacity. *J Mater Chem A*. 2013;1(6):2337-2342.
31. Wang X, Li W, Wang X, et al. Electrochemical properties of $NiCoO_2$ synthesized by hydrothermal method. *RSC Adv*. 2017;7(80):50753-50759.
32. Yan N, Hu L, Li Y, et al. Co_3O_4 nanocages for high-performance anode material in lithium-ion batteries. *J Phys Chem C*. 2012;116(12):7227-7235.
33. Yang Z, Qian K, Lv J, et al. Encapsulation of Fe_3O_4 nanoparticles into N, S co-doped graphene sheets with greatly enhanced electrochemical performance. *Sci Rep*. 2016;6(1):1-10.
34. Xiao P, Shi M, Xu L, et al. An efficient chemical reduction-induced assembly of Fe_3O_4@graphene fiber for wire-shaped supercapacitors with ultrahigh volumetric energy density. *Sci China Technol Sci*. 2021;64(10):2246-2254.
35. Liang J, Kong J, Zhang J. Hollow concave zinc-doped Co_3O_4 nanosheets/carbon composites as ultrahigh capacity anode materials for lithium-ion batteries. *ChemElectroChem*. 2021;8(1):172-178.
36. Pang M, Long G, Jiang S, et al. Ethanol-assisted solvothermal synthesis of porous nanostructured cobalt oxides (CoO/Co_3O_4) for high-performance supercapacitors. *Chem Eng J*. 2015;280:377-384.
37. Park SK, Kim JK, Kang YC. Excellent sodium-ion storage performances of $CoSe_2$ nanoparticles embedded within N-doped porous graphitic carbon nanocube/carbon nanotube composite. *Chem Eng J*. 2017;328:546-555.
38. Park SK, Park JS, Kang YC. Selenium-infiltrated metal–organic framework-derived porous carbon nanofibers comprising interconnected bimodal pores for Li–se batteries with high capacity and rate performance. *J Mater Chem A*. 2018;6(3):1028-1036.
39. Oh HG, Yang SH, Kang YC, Park SK. N-doped carbon-coated $CoSe_2$ nanocrystals anchored on two-dimensional MXene nanosheets for efficient electrochemical sodium-and potassium-ion storage. *Int J Energy Res*. 2021;45(12):17738-17748.
40. Wang B, Tang Y, Lu XY, et al. Rectangular Co_3O_4 with micro−/nanoarchitectures: charge-driven PDDA-assisted synthesis and excellent lithium storage performance. *Phys Chem Chem Phys*. 2016;18(6):4911-4923.
41. Yoon T, Kim J, Kim J, Lee JK. Electrostatic self-assembly of Fe_3O_4 nanoparticles on graphene oxides for high capacity lithium-ion battery anodes. *Energy*. 2013;6(9):4830-4840.
42. Zhu S, Fan L, Lu Y. Highly uniform Fe_3O_4 nanoparticle–rGO composites as anode materials for high performance lithium-ion batteries. *RSC Adv*. 2017;7(87):54939-54946.
43. Wang N, Liu Q, Sun B, et al. N-doped catalytic graphitized hard carbon for high-performance lithium/sodium-ion batteries. *Sci Rep*. 2018;8(1):1-8.
44. Jo MS, Ghosh S, Jeong SM, Kang YC, Cho JS. Coral-like yolk–shell-structured nickel oxide/carbon composite microspheres for high-performance Li-ion storage anodes. *Nanomicro Lett*. 2019;11(1):1-8.
45. Klink S, Ventosa E, Xia W, La Mantia F, Muhler M, Schuhmann W. Tailoring of CNT surface oxygen groups by gas-phase oxidation and its implications for lithium ion batteries. *Electrochem Commun*. 2012;15(1):10-13.
46. Luo L, Wu J, Xu J, Dravid VP. Atomic resolution study of reversible conversion reaction in metal oxide electrodes for lithium-ion battery. *ACS Nano*. 2014;8(11):11560-11566.
47. Shen Y, Shen X, Yang M, et al. Achieving desirable initial coulombic efficiencies and full capacity utilization of li-ion batteries by chemical prelithiation of graphite anode. *Adv Funct Mater*. 2021;31:2101181.
48. Kim JK, Park SK, Park JS, Kang YC. Uniquely structured composite microspheres of metal sulfides and carbon with cubic nanorooms for highly efficient anode materials for sodium-ion batteries. *J Mater Chem A*. 2019;7(6):2636-2645.
49. Gao M, Bao Y, Qian Y, Deng Y, Li Y, Chen G. Porous anatase-TiO2 (B) dual-phase nanorods prepared from in situ pyrolysis of a single molecule precursor offer high performance lithium-ion storage. *Inorg Chem*. 2018;57(19):12245-12254.
50. Jeong SY, Cho JS. Porous hybrid nanofibers comprising $ZnSe/CoSe_2$/carbon with uniformly distributed pores as anodes

for high-performance sodium-ion batteries. *Nanomaterials*. 2019;9(10):1362.

51. Luo W, Li F, Gaumet JJ, et al. Bottom-up confined synthesis of nanorod-in-nanotube structured Sb@ N-C for durable lithium and sodium storage. *Adv Energy Mater*. 2018;8(19):1703237.
52. Seon YH, Kang YC, Cho JS. One-dimensional porous nanostructure composed of few-layered $MoSe_2$ nanosheets and highly densified-entangled-N-doped CNTs as anodes for Na ion batteries. *Chem Eng J*. 2021;425:129051.
53. Oh SH, Park SM, Kang DW, Kang YC, Cho JS. Fibrous network of highly integrated carbon nanotubes/MoO_3 composite bundles anchored with MoO_3 nanoplates for superior lithium-ion battery anodes. *J Ind Eng Chem*. 2020;83:438-448.

SUPPORTING INFORMATION

Additional supporting information may be found in the online version of the article at the publisher's website.

How to cite this article: Nam KC, Seon YH, Bandyopadhyay P, Cho JS, Jeong SM. Porous nanofibers comprising hollow Co_3O_4/Fe_3O_4 nanospheres and nitrogen-doped carbon derived by Fe@ZIF-67 as anode materials for lithium-ion batteries. *Int J Energy Res*. 2022;46(7):8934-8948. doi:10.1002/er.7770